# The contribution of swelling to self-sealing of claystone studied through x-ray tomography

Alice Di Donna, Pascal Charrier, Jelke Dijkstra, Edward Andò, Pierre Bésuelle

## ▶ To cite this version:

Alice Di Donna, Pascal Charrier, Jelke Dijkstra, Edward Andò, Pierre Bésuelle. The contribution of swelling to self-sealing of claystone studied through x-ray tomography. Physics and Chemistry of the Earth. Parts A/B/C, 2022, 127, pp.103191. 10.1016/j.pce.2022.103191 . hal-03740695

**HAL Id: hal-03740695**

**https://hal.univ-grenoble-alpes.fr/hal-03740695v1**

Submitted on 29 Jul 2022

# The contribution of swelling to self-sealing of claystone studied through x-ray tomography

*Alice* Di Donna[1], *Pascal* Charrier[1], *Jelke* Dijkstra[2], *Edward* Andò[1], *Pierre* Bésuelle[1]

[1] Univ. Grenoble Alpes, CNRS, Grenoble INP, 3SR, 38000 Grenoble, France
[2] Chalmers University of Technology, Gothenburg, Sweden

**Abstract.** Many countries, as among others France, Belgium and Switzerland, are facing the issue of finding a proper solution to store radioactive waste coming from nuclear power plants. The possibility to store them in underground tunnels is largely considered and investigated. In France, Andra (Agence Nationale pour la gestion des Déchets RAdioactifs) selected the Callovo-Oxfordian clay rock situated in the Meuse/Haute Marne site between 400 and 600 m depth as possible host rock deposit. The excavation of the storage tunnels is expected to create a fractured zone around galleries. The factures will be then gradually re-saturated by the underground water coming from the surrounding rock and they are expected to self-seal in contact with water, thanks to the swelling potential of COx. The capacity of self-sealing, *i.e.* closing of fractures after water contact and possibly restoring of permeability, is thus of primary interest for the safety of the storage system with respect to water, gas and solutes transport. The physical mechanisms driving this phenomenon are mainly the swelling and de-structuration of the clay matrix present in the claystone. In this work, the self-sealing response of COx was investigated through x-ray tomography at multi-micrometre and sub-micrometre voxel size. The objective was to study the influence of mineralogy, size of the discontinuity, hydraulic paths, mutual orientation of the bedding plane and fractures. The size of the discontinuity is of primary importance in determining the percentage of closure. Fractures parallel to the bedding plane are more likely to seal as swelling is anisotropic and occurs mainly perpendicular to the bedding plane. The main novelty is represented by the direct and local observation of the physical process of self-sealing down to a scale lower than 1 μm.

**Keywords.** Claystone; self-sealing; x-ray tomography; swelling; anisotropy.

## 1 Introduction

Many countries, as among others France, Belgium and Switzerland, are currently facing the issue of finding a proper solution to store radioactive waste coming from nuclear power plants. As an example, in France, there are currently more than 50 operational nuclear power plants (among the largest there are those of Gravelines, Paluel, Cattenom, etc..). The 90% of the produced wastes, i.e. those characterised by a low or medium radioactive level, are nowadays stored in three surface industrial plants, two actives in the Aube region and one almost closed in the north Cotentin area. The other 10% are high radioactive level wastes, which are temporary stored in specific and safe installations on the production sites, waiting for a more sustainable and long term solution. At the international scale, the other countries are experiencing similar situations. A complete international summary of the current situation can be found on the Andra web site (www.andra.fr). The possibility to store the high radioactive level wastes in deep underground repository is largely considered and investigated. In this framework, the comprehension of the geological host formations behaviour is mandatory to ensure the long-term safety of the facility. Argillaceous formations are considered suitable as host rock in several countries (France, Belgium, Switzerland, *etc.*) for many reasons, among which the low hydraulic conductivity associated to high retention capacity for radionuclides (uranium and platinum) and the limited number of hydraulically active fractures. However, it is well known that the drilling of the access and repository tunnels induces a so-called Excavation Damaged Zone (EDZ) around the gallery section, characterised by a network of fractures that may become preferential hydraulic paths within the host rock. The permeability of this zone with respect to water, gas and solutes transport might increase of several orders of magnitudes (Bossart et al. 2002).

However, the hydro-mechanical *in-situ* conditions after the closure of the repository combined with the peculiar behavioural features of such argillaceous formations might be favourable for, at least partial, closure of open fractures and consequent, at least partial, recovery of the permeability (self-sealing). This was confirmed by the *in-situ* experimental observations realised in the Underground Research Laboratories (URLs) built for this purpose in Meuse/Haute Marne in Eastern France (Delay et al. 2007), Mol in Belgium (Bernier et al. 2004) and Mont Terry in Switzerland (Alheid et al. 2004). The understanding of self-sealing mechanisms and their quantification is consequently an important factor to consider in the performance assessment for nuclear waste repository in clay formation. For this purpose, a number of experimental studies were also carried out at the laboratory scale on samples collected in the URLs and they pointed out that different mechanisms might contribute to the self-sealing of open fractures in clayey formations (Bernier et al. 2004, Davy et al. 2007, Zhang and Rothfuchs 2008):

(i) Mechanical induced closure (increase of normal stress, contracting behaviour during shearing, creep …);
(ii) Sedimentation combined with clogging by colloidal phases and precipitation of solutes;
(iii) Physico-chemical interaction between the clay particles and the pore water.

A complete summary of the conclusions drawn from literature on the different mechanisms is provided by Bock et al. (2010). The focus of this paper is to go a step further in the understanding of mechanism (iii), which appeared to be not completely understood. The innovative approach proposed here allows the direct and local observation of the evolution of the clay matrix during the self-sealing process at submicron scale. In this study, the tested material is the Callovo-Oxfordian claystone (COx), *i.e.* the geological formation selected by Andra (Agence Nationale pour la gestion des Déchets RAdioactifs) as host rock for nuclear waste disposal in France. The already mentioned Meuse/Haute Marne URL is built in the COx formation between 400 and 600 m depth. The main level of the URL consists of approximately 2 kilometres of tunnels at a depth of 490 m, in the so-called "clay-rich unit" (U A). Above this layer, from 450 to 470 m depth there is the so-called Transitional Unit (U.T.), over which a Silicate-Carbonate Unit (U.S.C.) lies. The three units differ in terms of mineralogical composition, the U.A. being richer in clays, the U.S.C. being richer in carbonates and the U.T. being a transitional zone between the two others (Conil et al. 2018). The very low permeability of the material from the U.A. in intact conditions is in the order of $10^{-20}$ $m^2$ (Davy et al. 2007, Distinguin and Lavanchy 2007).

In this paper, the self-sealing behaviour of COx induced by the physico-chemical interactions in the clay matrix was studied experimentally, through x-ray micro tomography and quantitative image analysis. This represents the main innovative aspect with respect to previous studies. First, the known physical mechanisms and assumptions regarding the peculiar clays behaviour and microstructure are recalled. They are thought to be the driving mechanisms of the observed behaviour. Then, the experimental protocol and methods adopted are described. Finally, selected results are presented and discussed in the framework of the physical mechanisms highlighted previously and based on mineralogical analyses performed to interpret them. The experimental campaign included samples coming from both the U.A. and U.T., prepared with different fractures sizes and orientations with respect to the bedding plane, to study the variability of the response.

## 2 Physical mechanisms behind self-sealing

The structure of COx at the micro and nano scale can be schematised as illustrated in Figure 1, where the nomenclature used in the following is also indicated for the sake of clarity. Clay minerals have a layered structure, which results from a combination of silicon tetrahedral (T) and aluminium or magnesium octahedral (O) sheets, forming in most of the cases either T-O-T (smectite or illite type) or T-O (kaolin type) layers (Mitchell and Soga 2005). Several layers form what is called a clay particle, which usually has thickness in the order of one μm or less.

The COx clay matrix is mainly composed by T-O-T layers, with an alternation of smectite (swelling clays), in which the T-O-T layers are separated by inter-layer (intra-particle) bounded water, and illite (non-swelling clays), in which the space between the T-O-T layers are filled by ions, usually potassium (Conil et al. 2018). The clay particles external surfaces are negatively charged, mainly because of the isomorphic substitution, which results in a high adsorption potential. Therefore, exchangeable cations and water molecules are attracted to the surface, resulting in an inter-particle externally bounded water layer. At a larger distance from the surface of the clay particles, water increasingly becomes more weakly bonded and then free.

Before the excavation of the repository tunnels, the rock mass is assumed to be in a hydro-mechanical equilibrium state, with a quasi-static distribution of bound and free water. The drilling induces a mechanical stress release and redistribution, which alters this equilibrium and leads to fractures formation. These are mainly traction and shear fractures close to the excavation and shear fractures only further from the drift. This might give rise to different scenarios:

- During the operational phase, inflow of air is coming from the tunnel ventilation, with possible drying of the lips of the fractures. After the closure of the repository, these dry fractures will be gradually re-saturated by the water coming from the host rock;
- Redistribution of bounded and free water, with possible inflow of water having different chemistry. This is promoted by the increased permeability, as well as by the osmotic gradients appearing because of the creation of new particles surfaces, which act as driving forces.

Smectite clays are highly sensitive to water, showing swelling and structural disintegration during hydration. Depending on the confinement conditions, the clay in contact with water either undergoes a volume increase (unconfined conditions) or develops a swelling pressure (constant volume or partially confined conditions). In the case of COx, experimental tests performed by Zhang et al. (2007) show that the unconfined volumetric expansion reaches up to 8-12% and the swelling pressure is in the order of 10 MPa, varying depending on the confinement conditions. At the microstructural level, swelling is driven by electro-static mechanisms including (i) water absorption between the clay layers (inter-layer, intra particles) due to hydration of the exchangeable cations and (ii) water adsorption between the clay particles (inter particles) due to water interaction with the negatively charged particles surface. Swelling and possible structural disintegration due to fractures resaturation or water redistribution after the closure of the repository are considered to contribute significantly to fractures self-sealing. An analysis of these phenomena is the main goal of the experimental campaign described in this paper.

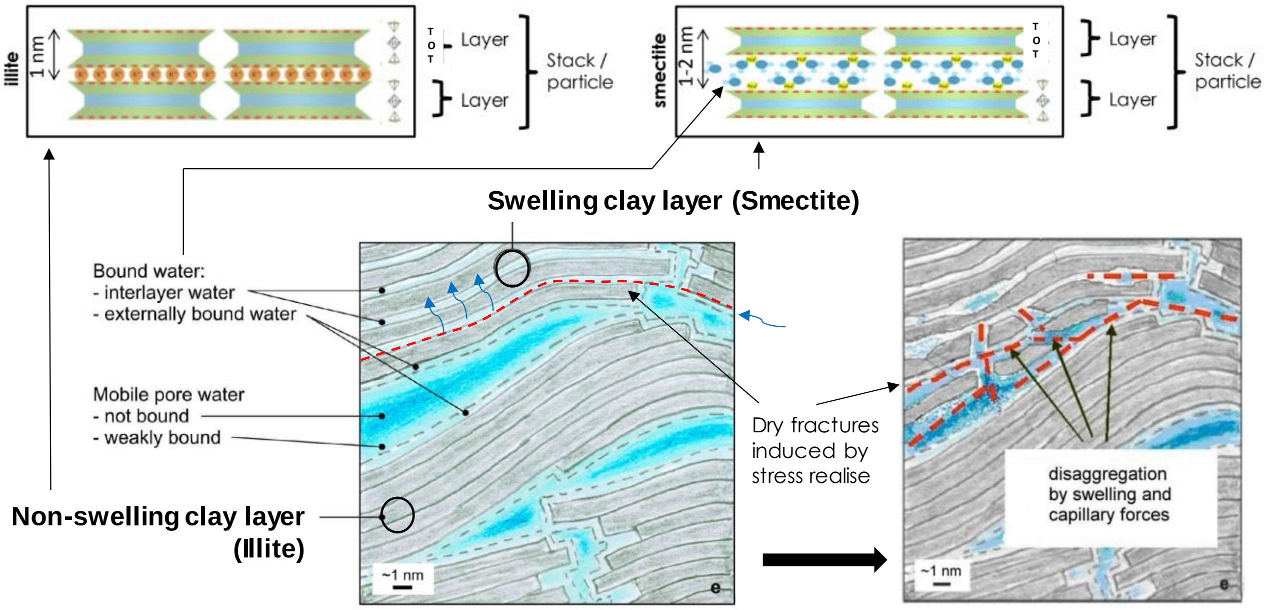

**Figure 1. Schematic representation of COx microstructure and physico-chemical self-sealing inducing mechanisms (adapted from Bock et al., 2010).**

## 3 Tested material

Samples collected in both the U.A. (cores EST53644 and EST58102) and the U.T. (cores EST57243 and EST57261) were tested in this work. The initial void ratio, water content and degree of saturation of the COx cores as received from the site are presented in Figure 2 (triangles), together with data collected from other studies on the same material (Pham et al. 2007, Mohajerani et al. 2011, Wan et al. 2013, Conil et al. 2018, Stavropoulou et al. 2018). Here, the void ratio was measured in the laboratory through the Archimedes' technique, the water content was measured through oven drying at 105 °C for 24 hours and the degree of saturation was computed knowing that the specific density of COx is $G_s$=2.7. Combining these data, it appears that the in-situ water content of COx generally ranges between 6 and 8 % in the U.A, with the void ratio varying between 0.12 to 0.28.

The U.T. samples showed much lower initial water content (in the order of 1.5 to 2 %), which was associated to the very low void ratios. This might be not representative of the whole unit, but only of the cores tested in this paper. More data regarding the water content, void ratio and degree of saturation of all strata were provided by Conil et al. (2018).

The mineralogy of the material coming from the U.A. is well known in the literature: it is composed by a clay fraction (phyllosilicates) of 42% ± 11%, a carbonates content of 30% ± 12%, a tectosilicates content of 25% ± 8%, and the other ancillary minerals constitute less than 4% (Conil et al., 2018). To compare these data with those related to the material coming from the U.T., x-ray diffraction mineralogical analyses were performed in this study on two samples collected respectively from cores EST57243 and EST57261. These analyses were carried out at the institute ISTerre (Grenoble, France). The results were obtained through the Rietveld method, after identification of the different phases present in the samples. The amorphic phases were not determined. The results are presented in Table 1 together with those of the U.A. from the literature. The uncertainty on the U.T. samples analyses is in the order of ± 1-2%.

The material from core EST57261 presented an extremely high carbonates content (78.1%) and a low clay content (around 9.5% with smectite around 5.9%) and tectosilicate (11.8%) content. The strong presence of carbonates is coherent with the very low void ratio measured in the laboratory. The material from EST57243 had a carbonates content of 38%, lower than EST57261 but still higher than the average values in the U.A. The clay content is also slightly higher (25.7%), but still lower than the one of the U.A material. This is also consistent with the measured values of void ratio.

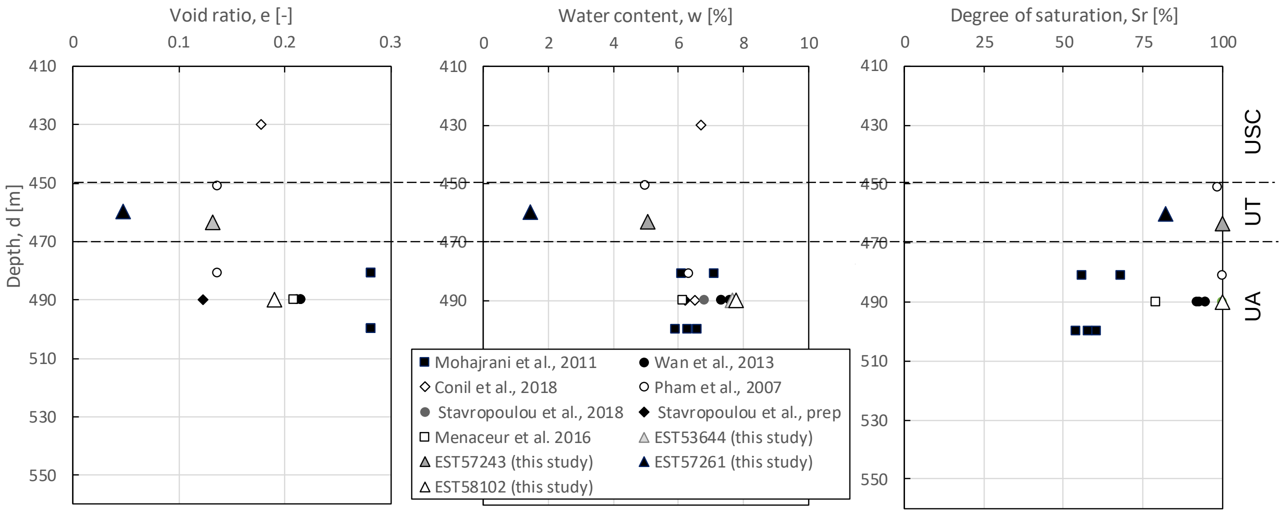

**Figure 2. Initial void ratio, water content and degree of saturation of the tested samples, compared with data from literature on the same material.**

**Table 1. Mineralogical x-ray diffraction analyses on U.T. samples compared with those of the U.A. material from literature.**

| **Phase** | | **U.A. (Conil et al. 2018)** | **EST57243 (this study)** | | **EST57261 (this study)** | |
|---|---|---|---|---|---|---|
| **Tectosilicates** | Quartz | 25 % | 25.2 % | 34.7 % | 8.5 % | 11.8 % |
| | Plagioclase | | 1.7 % | | - | |
| | Feldspath K | | 7.8 % | | 3.3 % | |
| **Carbonates** | Calcite | 30 % | 33.2 % | 38.0 % | 76.5 % | 78.1 % |
| | Ankerite | | 2.4 % | | 1.6 % | |
| | Dolomite | | 2.4 % | | - | |
| **Clay** | Smectite | 42 % | 11.9 % | 25.7 % | 5.9 % | 9.5 % |
| | Mica | | 12.0 % | | 3.3 % | |
| | Chlorite | | 1.8 % | | 0.3 % | |
| **Others** | Pyrite | < 4 % | 0.8 % | 1.1 % | 0.4 % | 0.4 % |
| | Anatase | | 0.3 % | | - | |

## 4 Experimental campaign

The experimental procedure adopted is described hereafter, from the sample preparation, to the tests program and the description of the used device. The results are presented in the next sections, starting from those obtained on the samples from the shallowest units and going deeper up to those representatives of the U.A.

### 4.1 Samples preparation

The samples with height of 20 mm and diameter between 8 and 9 mm, were cut from the cores received from the site, by means of a diamond wire saw. The complete sample preparation procedure is illustrated in Figure 3. The cores were firstly scanned through x-ray tomography to identify the most suitable areas, which were selected as those with the minor number of cracks and large inclusions (an example for core EST57261 is shown in Figure 3a). Slices were cut from the cores (Figure 3b), in the selected zones, having either thickness of 20 mm (to cut samples with their axis parallel to the axis of the core) or 30 mm (to cut samples having their axis perpendicular to the axis of the core). Accordingly, the cylindrical samples were cut with various orientations with respect to the in-situ bedding plane (*i.e.* with respect to the *in-situ* principal stresses direction) in order to investigate the effect of fabric anisotropy on the material response (Figure 3c). An indication of the *in-situ* orientation of the cores with respect to the bedding plane was provided by Andra. Each sample was then cut in two semi-cylinders in order to create an artificial discontinuity (Figure 3d). Finally, each semi-cylinder was glued on a semi-cylindrical shell (Figure 3e). The two half-shells were glued together, separated by a spacer controlling the size of the artificial discontinuity. The shells containing the sample were then positioned in the experimental device (see later) for scanning through x-ray tomography (Figure 3f).

Total suction and water content were also measured at different stages during samples preparation on a parallel series of specimens subjected to the same preparation procedure as those that were  tested, in order to monitor their hydraulic state from the core opening to the beginning of the experiments. The suction measurements were done through the filter paper technique, using Whitman 42 filter papers (Kim et al. 2016). In Figure 4, these data are compared with the measurements provided by Wan et al. (2013) for the same material. The retention behaviour of the samples obtained from cores EST53644, EST58102 (U.A.) and EST57243 (U.T.) was consistent with those found in the literature. However, the behaviour of samples from EST57261 (U.T.) was substantially different. This is consistent with the discussed observations regarding the low initial void ratio and water content (Figure 2), as well as the high carbonates content (Table 1).

Despite the attention paid during the sample preparation procedure, the water loss appeared to be significant. For this reason, the samples were re-equilibrated before testing in a chamber with controlled temperature of 30 °C and relative humidity of 90% for 48 hours.

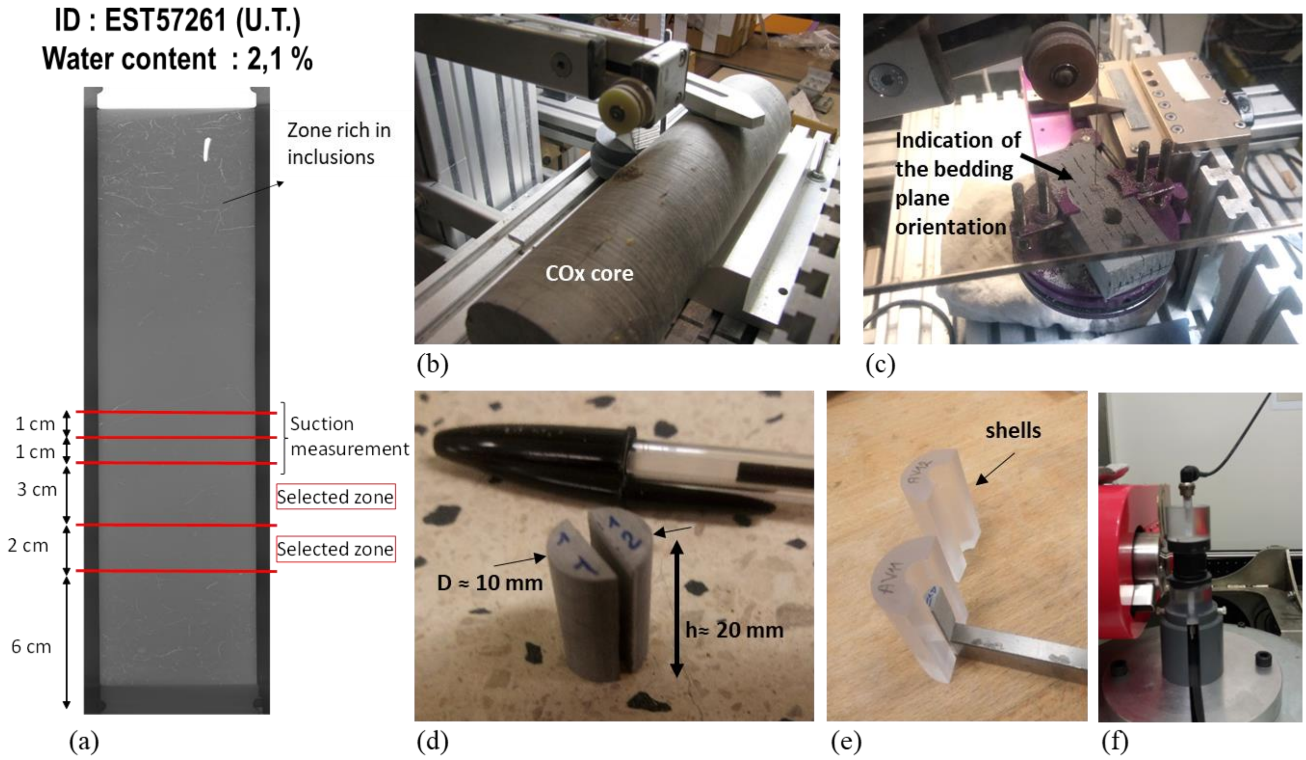

**Figure 3. Sample preparation procedure: (a) Initial whole core x-ray scan, (b) cut of slices, (c) cut of cylinders, (d) cut of the artificial discontinuity, (e) positioning of the sample into the shells, (f) positioning of the sample in the tomograph.**

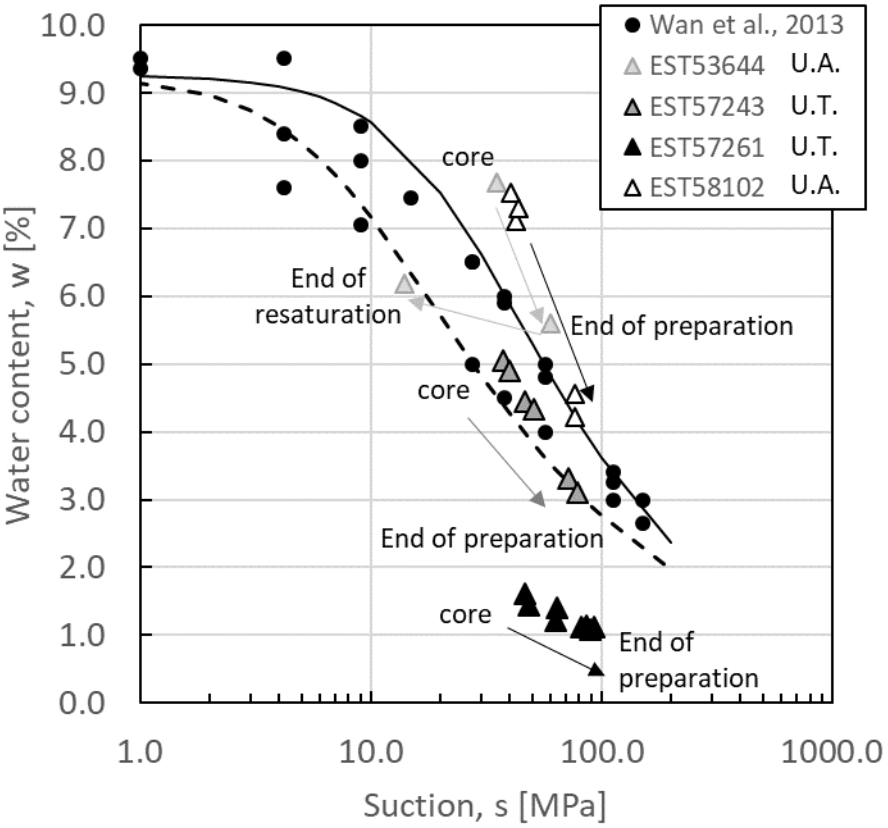

**Figure 4. Suction measurements at different stages during samples preparation and comparison with data from the literature.**

## 4.2 Testing program

A summary of the performed tests with the corresponding experimental conditions is provided in Table 2. Samples 3132, 4142, 8182 and 9192 were cut from core EST53644 (U.A. at around 490 m depth), samples AH1112 and AV1112 from core EST57243 (U.T. at around 463 m depth), samples BH4142 and BV3132 from core EST57261 (U.T. at around 460 m depth) and samples V3132, V4142 and H2122 from core EST58102 (U.A. at around 490 m depth). The orientation of each sample with respect to the bedding plane are also indicated, according to the notation illustrated in Figure 5. The loading path imposed in each test is a combination of three possible loading conditions, *i.e.* the discontinuity was either saturated by water vapour, or by liquid water or dried by dry air circulation. Varying discontinuity sizes ranging between 75 and 490 μm were tested. The opening and closure of the discontinuity during the different phases was monitored by x-ray tomography, regularly scanning the samples. Each scan is labelled with V, W or D, depending on the loading condition (V=water vapour, W=liquid water, D=drying), and numbered sequentially. The first eight experiments in Table 2 were carried out using the tomograph at Laboratoire 3SR (Viggiani et al. 2015), in Grenoble (France). The last three tests were performed at the ID19 beamline at the European Synchrotron Radiation Facility (ESRF), also in Grenoble. In this case, the much higher brilliance allows higher spatial resolution and shorter scans. Consequently, higher frequency scanning was possible especially during the saturation by water phases, when the material was expected to react faster. The scans are reconstructed with Paganin Phase retrieval to increase contrast. In all testing phases, the duration of each scan was chosen according to the material's reaction rate, thus being faster at the beginning of the experiment (to the detriment of the resolution) and gradually slower as the process evolved with time. The fastest scans in the Laboratoire 3SR were 10 minutes long, with a voxel size of 15 μm (binning 2) or 7.5 μm (no binning), while at ID19 a voxel size of 0.7 μm (local tomography on a partial zone of the specimen) was obtained for a scan duration of 5 minutes. Quantitative full-field measurements of the kinematics between volume reconstructions have been performed with the digital volume correlation code SPAM (Stamati et al., 2020). The correlation window size was 21x21x21 voxels and the window spacing was 20 voxels size.

**Table 2. Experimental program.**

| Core | Test | Geological unit | Bedding plane | Loading path | Fracture size [μm] |
|---|---|---|---|---|---|
| EST53644 | 3132 | U.A. (490 m depth) | Axial (fracture angle ≈ 30°) | V-W-D | 75 |
| EST53644 | 4142 | U.A. (490 m depth) | Axial (fracture angle ≈ 30°) | V-W-D | 150 |
| EST53644 | 8182 | U.A. (490 m depth) | Axial (fracture angle ≈ 30°) | D-W | 300 |
| EST53644 | 9192 | U.A. (490 m depth) | Axial (fracture angle ≈ 30°) | D-W | 425 |
| EST57243 | AH1112 | U.T. (463 m depth) | Ortho-axial | V-W | 430 |
| EST57243 | AV1112 | U.T. (463 m depth) | Axial (parallel) | V-W | 240 |
| EST57261 | BH4142 | U.T. (460 m depth) | Ortho-axial | V-W-D | 490 |
| EST57261 | BV3132 | U.T. (460 m depth) | Axial (parallel) | V-W | 165 |
| EST58102 | V3132 | U.A. (490 m depth) | Axial (perpendicular) | W | not regular |
| EST58102 | V4142 | U.A. (490 m depth) | Axial (parallel) | W | 75 |
| EST58102 | H2122 | U.A. (490 m depth) | Ortho-axial | W | 300 |

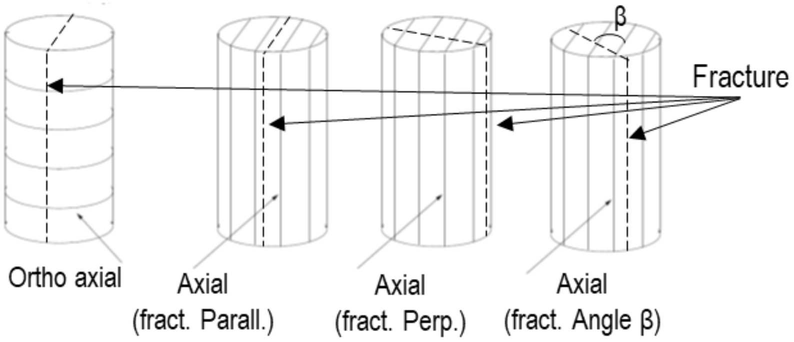

**Figure 5. Orientation of the samples and the artificial discontinuity with respect to the in-situ bedding plane.**

## 4.3 Experimental setup

The experimental setup is presented in Figure 6. The polycarbonate shells containing the samples were placed between a base and a top cap, which were connected to a circuit including a pump and a reservoir. The pump circulates the dry air (RH<20%), water vapour (RH>96%) or liquid water contained in the reservoir to the sample discontinuity, from the bottom to the top. A sensor is used to monitor the relative humidity and temperature in the reservoir. During the phases of saturation by liquid water, the water was pumped up to fill completely the discontinuity, without continuing circulation to reduce the risk of material erosion. Synthetic water prepared in the laboratory according to the *in-situ* salinity was used (Table 3, Leroy et al. 2007). During the drying phases, calcium chloride salt ($CaCl_2$) was used in the reservoir to dry the air, thanks to its hygroscopic behaviour. An external soft membrane was used around the shells to ensure sealing during saturation by water phases (Figure 3f).

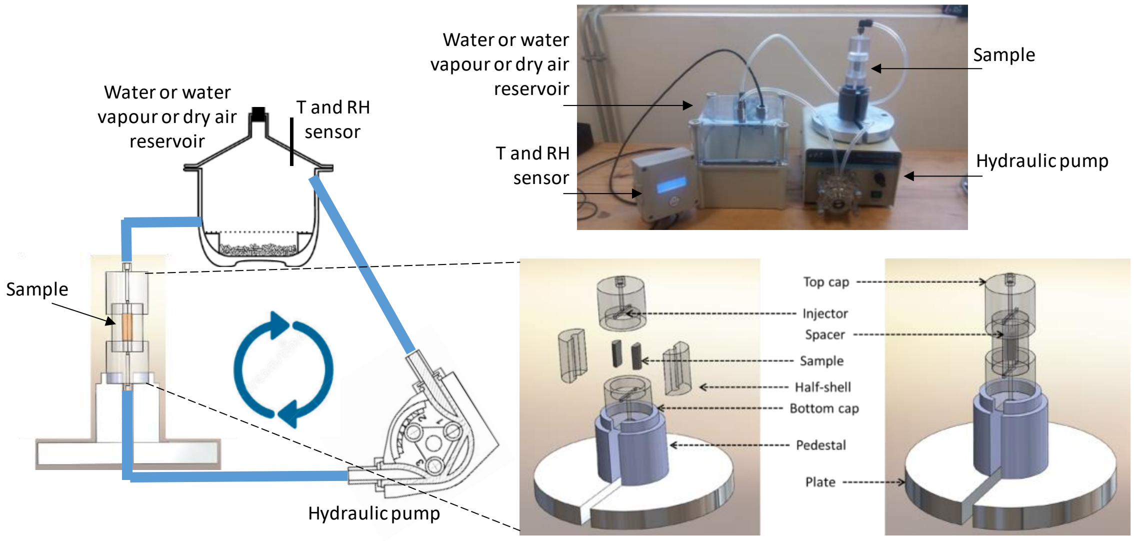

**Figure 6. Experimental setup.**

**Table 3. In-situ water salinity reproduced in the experiments.**

| Salt | Quantity [g/l] |
|---|---|
| NaCl | 1.950 |
| $NaHCO_3$ | 0.130 |
| KCl | 0.035 |
| $CaSO_4,2H_2O$ | 0.630 |
| $MgSO_4,7H_20$ | 1.020 |
| $CaCl_2,2H_2O$ | 0.080 |
| $Na_2SO_4$ | 0.700 |

## 5 Results in the U.T. at 460 m depth

Figure 7 shows the central slice (middle height of the sample) at different steps during the experiment, for sample BH4142. The presented steps are those at the end of each testing phase (V-W-D). No remarkable reaction was detected with the naked eye in any of the testing phases, at least at this resolution and for the duration of the test.

Figure 8 shows comparable results for sample BV3132. In this case, due to the limited reaction of the sample, the decision was taken to extend the W-phase to the detriment of the D-phase, which was not performed: thus, images are presented for the initial state before the beginning of the test, at the end of the V-phase and after 0.5 and 2 days of W-phase. Again, no reaction was discerned with the naked eye.

The initial results were unexpected, especially if compared with the quite fast and evident reaction of the samples coming from the U.A. (see section 7), as well as based on the literature. This was the incentive to make the x-ray diffraction mineralogy analyses (Table 1) to compare the composition with that of the U.A. material (Conil et al. 2018). The mineralogy analyses indicate that the absence of reaction is potentially linked to the combination of very low clay content and small void ratio due to the very high carbonates content, which prevents the water to penetrate the sample.

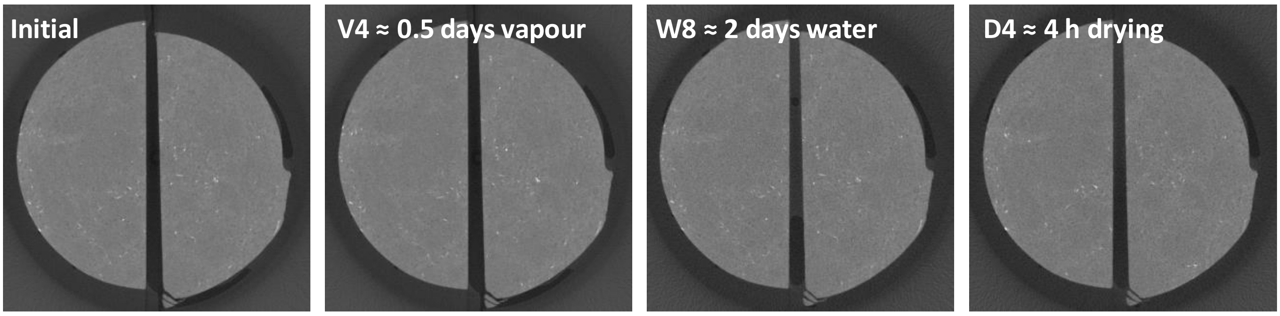

**Figure 7. X-ray images at different steps during test BH4142 (U.T.), middle slice, voxels size 15 μm. Initial mean gap is 490 μm.**

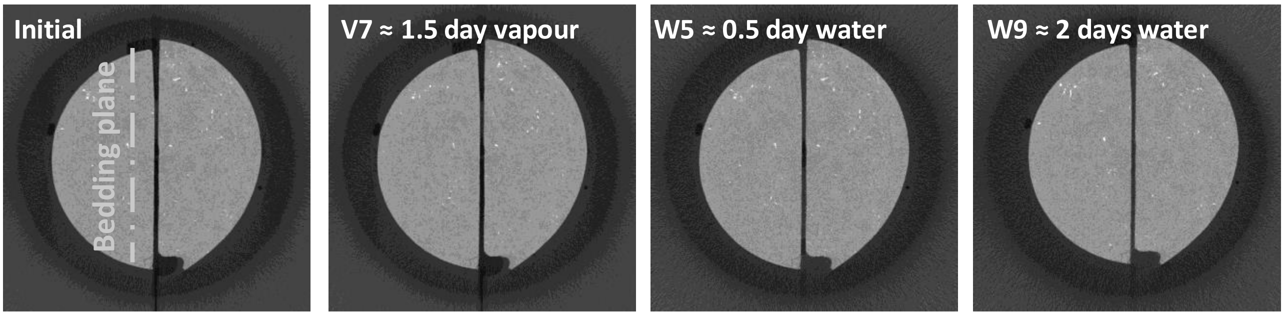

**Figure 8. X-ray images at different steps during test BV3132 (U.T.), middle slice, voxels size 15 μm. Initial mean gap is 165 μm.**

## 6 Results in the U.T. at 463 m depth

Figure 9 shows the central slice (middle height of the sample) of sample AH1112 before the start of the test, after 1.5 days of saturation by water vapour and after 2 and 4 days of saturation by liquid water. As before, also in this case the D-phase was omitted in order to extend the W-phase to the maximum time available. The low rate of the phenomenon enabled longer scans with improved resolution (voxel size 7.5 μm). Despite this, the reaction to both water vapour and liquid water was still very limited or at least invisible from visual inspection of the image data. However, analysing the result on the second sample coming from the same core (AV1112) but prepared with the artificial discontinuity parallel to the bedding plane, a modest closure was observed (Figure 10). In this case, only images from the saturation by liquid water are presented, as still no reaction was observed during the phase of saturation by water vapour. The fracture is far to be sealed, but its size reduces significantly in the duration of the experiment. To understand if the process was completed or still ongoing, further image analyses were carried out. The images were thresholded in the area around the fracture, with a threshold level corresponding to the average value of the two peaks of the grey level of the average histogram for the image stack in the selected sub volume (Figure 11), corresponding, respectively, to the water in the fracture and the solid part. A single threshold suitable for all test stages was identified. The fracture opening was estimated as the volume of the discontinuity (voxel counting) divided by the average height and width of the fracture. The result is represented in Figure 11b. This led to the conclusion that the process would have probably continued further (the duration of the W-phase was 4.5 days). At the end of the experiment, the average thickness of the discontinuity was reduced by more than 50%. The same procedure repeated for the test on sample AH1112 confirms a very limited evolution of the discontinuity size seen with the naked eye, with a maximum closure of less than 20 % of the initial fracture (the duration of the W-phase being 3 days). In this sense, the orientation with respect to the bedding plane plays an important role and the swelling of the material occurs preferably in the direction perpendicular to the bedding plane. With respect to samples BH4142 and BV3132 (section 5), the observed results are coherent with the different mineralogy, *i.e.* with the slightly higher clay content present in this case, associated with the lower carbonates content (Table 1). The two cores were collected at only three meters distance in depth, which may confirm the variability in space of the mineralogical conditions.

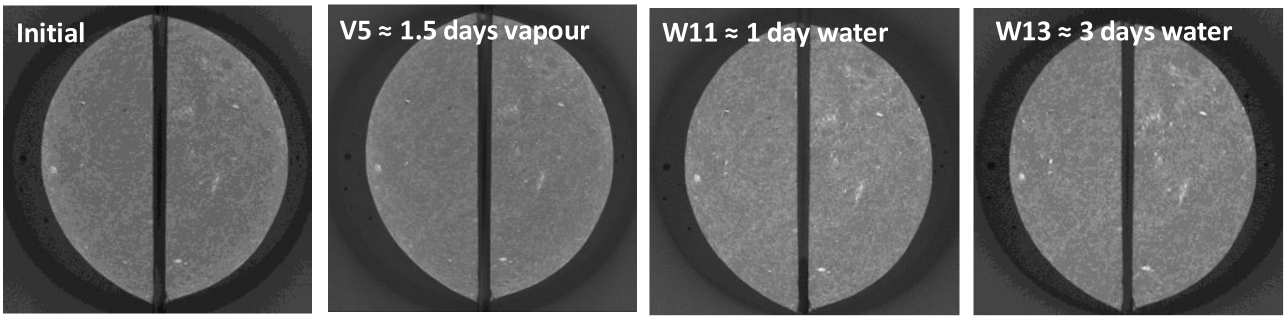

**Figure 9. X-ray images at different steps during test AH1112 (U.T.), middle slice, voxels size 7.5 µm. Initial mean gap is 430 µm.**

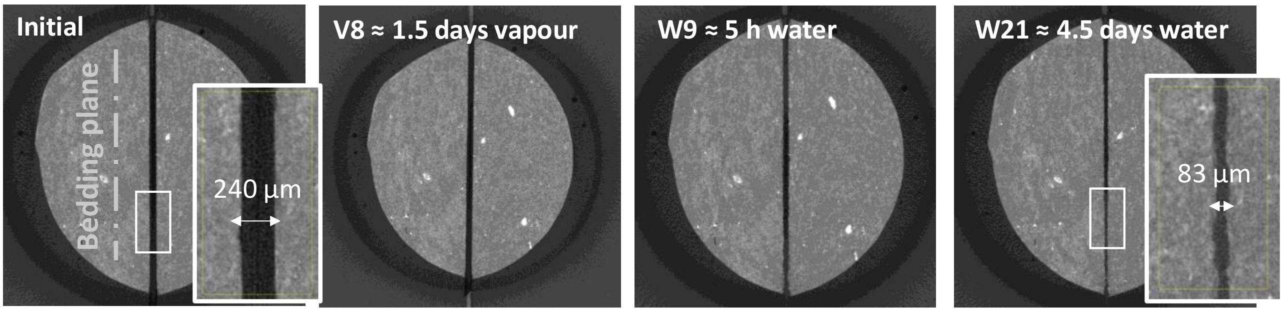

**Figure 10. X-ray images at different steps during test AV1112 (U.T.), middle slice, voxels size 7.5 µm. Initial mean gap is 240 µm (the thickness indicated are local values in the zoomed area).**

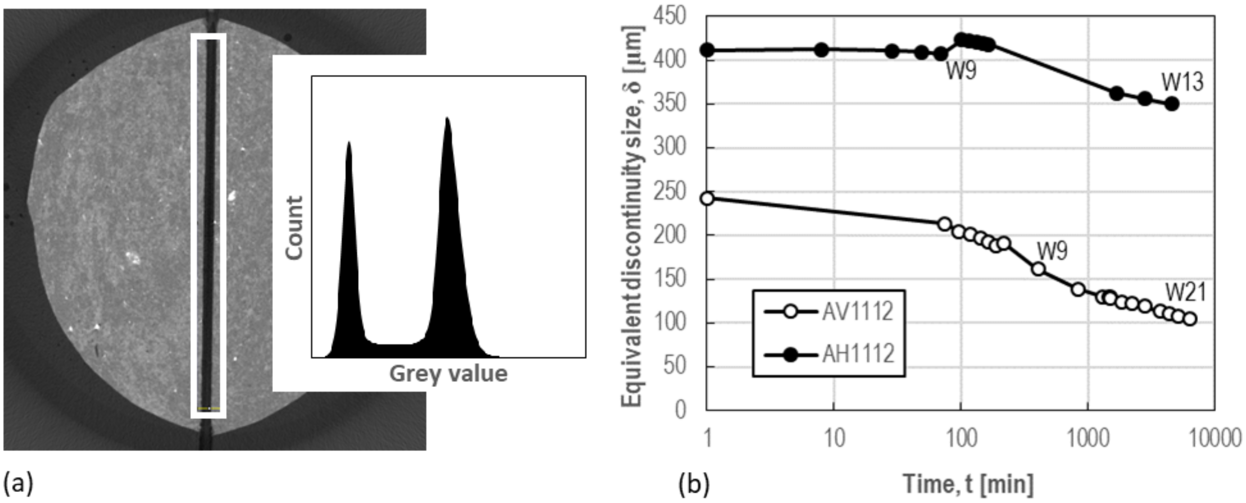

**Figure 11(a) Example of selected volume for thresholding (test AV1112) and typical related histogram; (b) Evolution of the equivalent size of the discontinuity during the tests AV1112 and AH112.**

## 7 Results in the U.A.

Figure 12 shows the central slice (middle height of the sample) for test 3132 before the beginning of test, after 10 minutes and 1 day of saturation by liquid water and after subsequent 3 days drying. Comparing with the reference scan obtained before the start of the experiment, the saturation by vapour phase does not present significant evolution so it was omitted here (see later). The sample reacted rapidly when it was put in contact with liquid water and the closure of the initial 75 µm discontinuity looked almost completed after a couple of hours, at least at the resolution of these images. The results for sample 4142 were comparable to those presented for test 3132.

Figure 13 shows the same kind of results for the test on sample 9192, before testing, at the end of the 1-day drying phase, and after 10 minutes and 6 hours of W-phase.

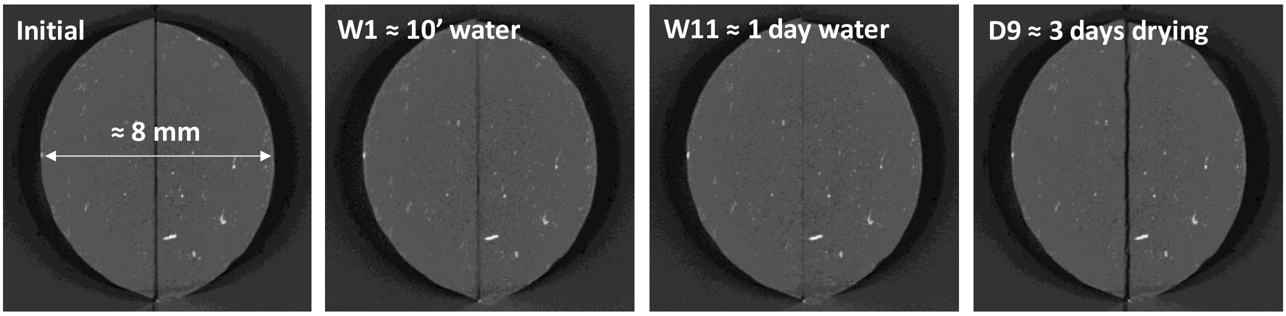

**Figure 12. X-ray images at different steps during test 3132 (U.A.), voxel size 13.5 µm. Initial mean gap is 75 µm.**

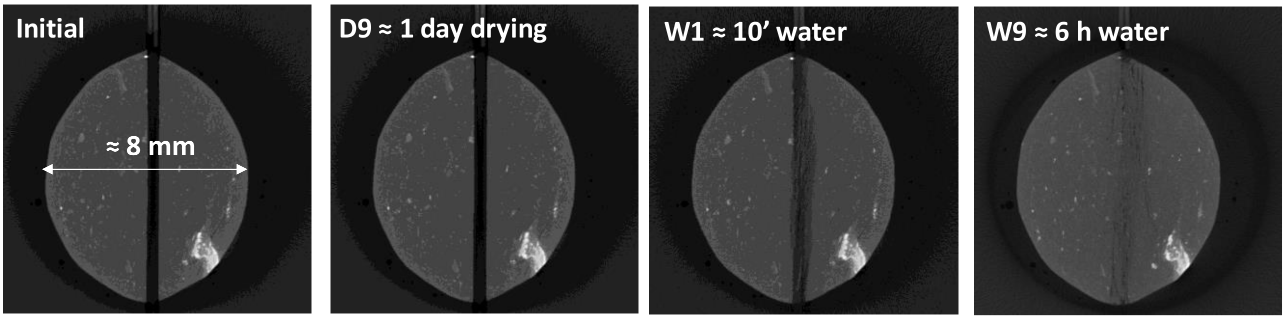

**Figure 13. X-ray images at different steps during test 9192 (U.A.), voxel size 15 µm. Initial mean gap is 425 µm.**

In this case, during the drying phase, the reaction was difficult to appreciate with the naked eye, but it was extremely rapid when the sample was put in contact with liquid water. With respect to tests 3132 and 4142, the initial size of the discontinuity was in this case larger (425 µm), and this wider space available, perhaps combined with the initial drying phase, amplified the swelling and de-structuring phenomena, leading to the formation of a visible peeling zone around the crack lips. In order to quantify the reaction in all the different testing phases, the same exercise described for sample AV1112 to study the evolution of the average thickness of the discontinuity was repeated for the four tests performed on U.A. samples. The results are presented in Figure 14a, b, c and d for test 3132, 4142, 8182 and 9192, respectively.

The vapour phases lasted two and one day, for test 3132 and 4142 respectively. The almost invisible reaction is confirmed by this more accurate analysis. In both cases, a small and slow closure is detected, between 5 and 10 µm. It might have been more significant for a longer test duration.

Conversely, when in contact with liquid water, the initial discontinuity closed rapidly, vanishing (less than 1 µm average value) after about 200-300 minutes for the small crack cases (test 3132 and 4142), and around 600 minutes for test 8182. The open space size in the last test (9192) looked larger even after stabilisation at 3280 minutes. This is likely due to the bigger initial size of the discontinuity. According to this analysis, with all the mentioned assumptions, the tests reached at the end a closure of more than 99% with respect to their aperture before the W-phase, except for test 9192, which reached 96%. Although the W-phase of test 9192 was the longest of the four, at the end, it had less closure. It is concluded that, for a given size of the specimens, the time needed to closure is linked to the initial size of the discontinuity, which seems to play the major role.

It is worth noting that all the quantitative results are related to the assumptions made in the thresholding method and on the image resolutions. Voids and cracks smaller than the voxel size are not detected. In this sense, a complete closure means the absence of detectable voids.

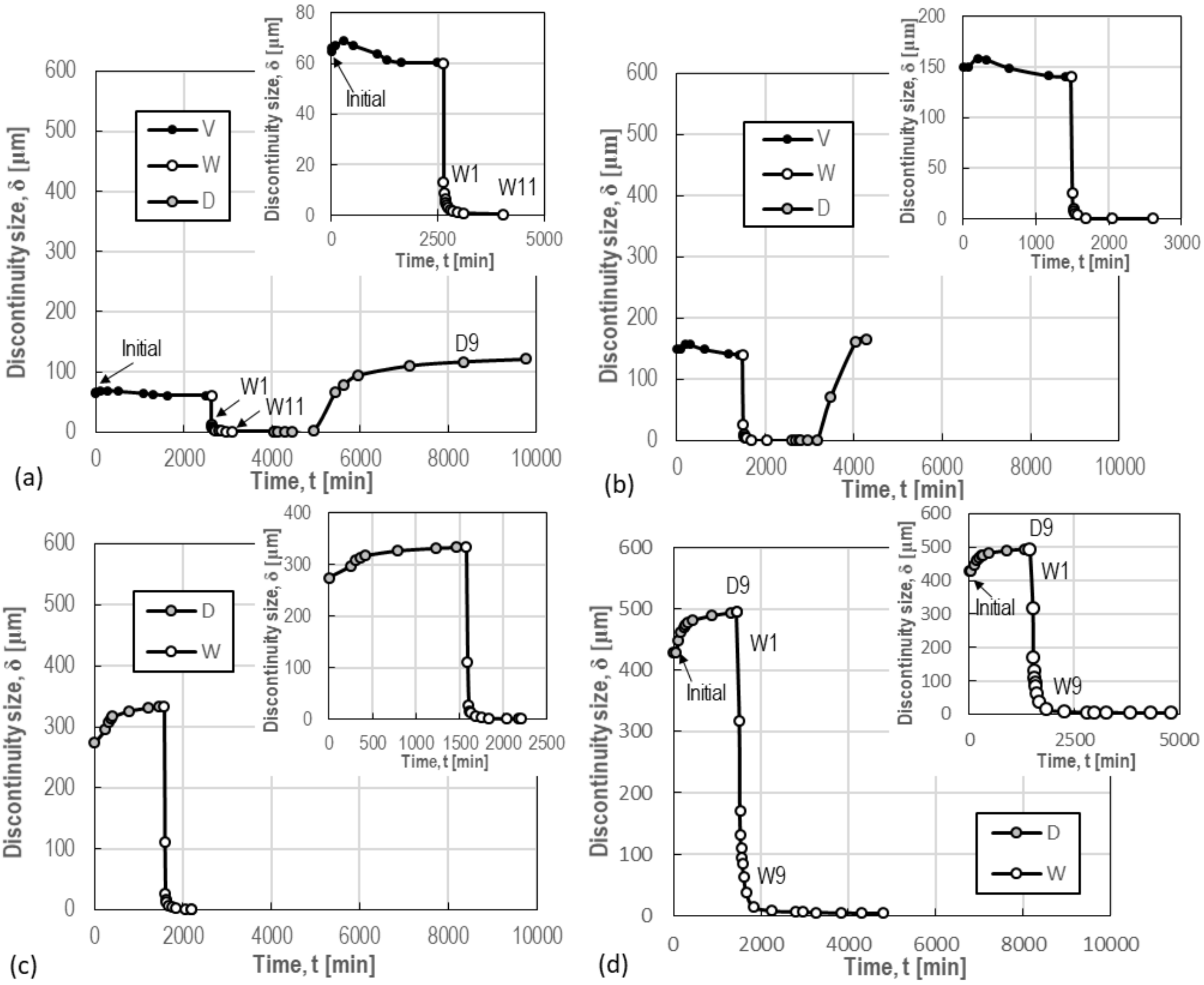

**Figure 14. Evolution of the average equivalent size of the discontinuity during test (a) 3132, (b) 4142, (c) 8182 and (d) 9192.**

During the drying phases, all the samples showed a significant opening of the fracture. This was clearly visible also with the naked eye for samples 3132 and 4142, which were subjected to drying after saturation (Figure 12). When drying was the first phase, the opening was less visible, but easily detected through the threshold method. Figure 15 compares the D-phases of the four tests in terms of discontinuity opening with time. Note that tests 3132 and 4142 are subjected to drying after a V- then W-phase, which means that the size of the crack before drying is close to zero. On the other hand, tests 8182 and 9192 starts directly with a D-phase, *i.e.* with an open fracture (300 and 425 µm respectively, see Table 2). The four curves show an initial opening rate in the order of 0.1-0.3 µm/min, and a second slower plateau-phase with an opening rate in the order of 0.001-0.004 µm/min. The opening rate of these two phases are common to all the tests. The main difference is that tests 3132 and 4142 (D-phase after V- then W- phases) keep the first opening rate for a longer period than tests 8182 and 9192 (D-phase as 1st step), ending up with an aperture twice (3132) and three times (4142) bigger than the two other samples.

Interestingly, through the threshold method, tests 3132 and 4142 show a final aperture after drying which is bigger than the initial one (Figure 14). This is likely related to the creation of a network of micro fissures around the initial discontinuity lips during the precedent saturation phase.

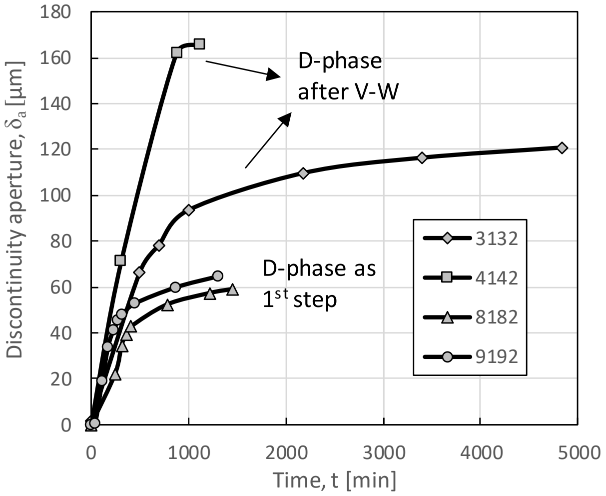

**Figure 15. Comparison of the D-phases of the four U.A. tests in terms of relative discontinuity aperture.**

### 7.1 Density evolution

In the absence of direct measurement of permeability, it was important to estimate the degree of healing, during the W-phases. At the near closure state, when the crack opening is smaller than the voxel size, the capacity of the former method based on grey level thresholding is limited and inaccurate. As the grey level is proportional to the bulk density of the material, the ratio of the grey level in the fracture zone to that of the intact material is used here as an indicator. Two volume selections were chosen for each test, one representative of the discontinuity and the other of the intact material. The evolution of the mean grey value in these two selected volumes was followed during the tests. The mean grey value of the intact material, is expected to remain quite constant, or it can slowly change due to eventual swelling and water resaturation (Stavropoulou et al. 2020). The grey level in the discontinuity is supposed to evolve from a value representative of air or vapour/liquid water (depending on the test) towards the one of the intact material. The discontinuity zone was selected to be entirely included in the empty area before the beginning of the tests, over the whole sample height. In this way, all the voxels included would be representative of the discontinuity. This is not always easy to achieve, especially for small fractures (*e.g.* in sample 3132), because of the not perfect verticality of the crack lips. This might be a source of inaccuracy in the measurement, which was verified to be in acceptable ranges. An example of the adopted procedure and obtained result is represented in Figure 16 for test 9192. In Figure 16a, the two selected zones are indicated on the axial vertical projection of the volume of the sample. In Figure 16b, the evolution of the mean grey value for the two selected volumes are presented during the test. As soon as the material starts to swell and the crack closes, the grey value increases sharply, while in the intact material outside the crack, the level drops very slightly. The intact rock target value was never achieved in the fracture at least in the considered test duration, meaning that in the fractured zone the initial intact condition is not completely recovered. This is likely related to the replacement of the main large fracture by a network of micro fractures, as discerned in the last image of Figure 13.

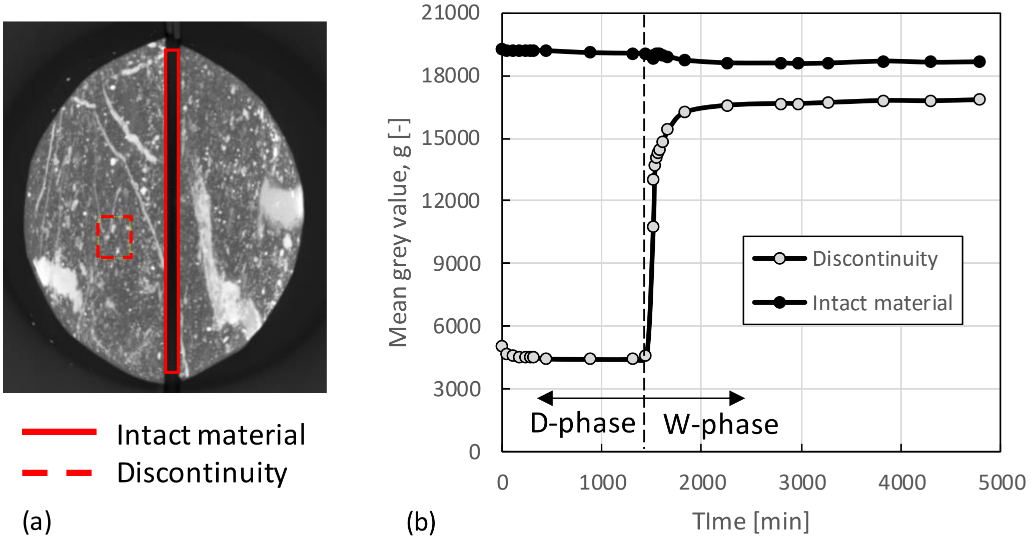

**Figure 16. Density study: (a) example of selection of the analysed zones on an axial projection of the volume of sample 9192, (b) evolution of the discontinuity area and intact material density during test 9192.**

To generalise this founding and compare the density evolution of the four tests carried out, a ratio R between mean grey values of the discontinuity and intact material zone was computed for each test as:

$$R = \frac{g_d}{g_i} * 100$$

where $g_d$ is the mean grey value of the discontinuity volume at the end of the W-phase and $g_i$ is the mean grey value of the intact material volume averaged over all the steps. The *R*-values obtained for the four tests are compared in Figure 17, as a function of the initial discontinuity size. It appears that the degree of recovery decreased with the increasing of the initial size of the discontinuity. The initial size of the discontinuity seems to play a primary role: the test with the larger initial discontinuity (test 9192) was the one with the lowest ratio R, even if it lasted longer than all the others did. It seems reasonable to conclude that the material has a maximum swelling potential. This could be related to the quantity of water available, the maximum number of water layers which can be adsorbed by the smectite particles (Saiyouri et al. 1998, Menaceur et al. 2016), but eventually also to the available material, which means in this case to the size of the sample. To understand better this phenomenon, x-ray micro tomography tests at higher resolution were performed. The results are discussed in the next section.

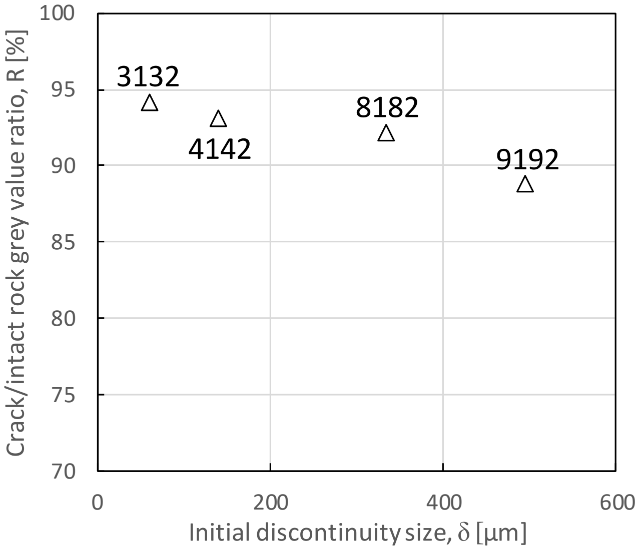

**Figure 17. R-values at the end of the W-phases for the four tests performed on the U.A. samples.**

## 7.2 High resolution images

For improved analyses of the physical phenomena driving the self-sealing behaviour of the material, three experiments on U.A. samples were repeated at a higher resolution (voxel size 0.7 µm) in beamline ID19 at the European Synchrotron Radiation Facility (ESRF), in Grenoble (France). The details of the experimental program are given in Table 2, the size of the specimens is the same as previously (about 10 mm diameter). One sample (H2122) was cut ortho-axial with respect to the in-situ bedding plane, while the two others (V3132 and V4142) were axial, respectively, with the fracture perpendicular and parallel to the bedding plane (Figure 5). The fracture size of sample H2122 was 300 µm, while the one of sample V4142 was around 75 µm. Sample V3132 resulted with a non-regular discontinuity due to technical problems during sample preparation. During each test, a scan session was performed every 15 minutes, including one "low-resolution" tomography (voxel size=6 µm) on the whole sample and two local high-resolution tomographies (voxel size=0.7 µm). These latter were focused on the discontinuity area, with a field view of about 2.6 mm in diameter: one perfectly centred on the discontinuity (labelled A) and the other slightly moved on the side (labelled B) to better analyse the diffusion of the phenomenon in the material (Figure 18). With respect to previous tests, in these ones a significantly higher spatial and temporal resolution was achieved, allowing gathering more information on the kinematic aspects of the studied phenomena. Figure 19, Figure 20 and Figure 21 show the central slice of samples H2122, V3132 and 4142, respectively, before the beginning of the tests, after 15 minutes and 1 hour of W-phase, and at the end of the experiment. Each test has a different duration, as it was stopped when the process was assumed stabilised. It appears that the bedding of sample H2122 is not exactly horizontal but rather inclined by 25° to the horizontal plane (Figure 19, bottom-left). As shown later, this appears to be important for understanding the process of crack sealing. Similarly, for sample V4142, the bedding is not exactly parallel to the crack but rather inclined by about 25° to the crack in the horizontal cut (Figure 21, top-left).

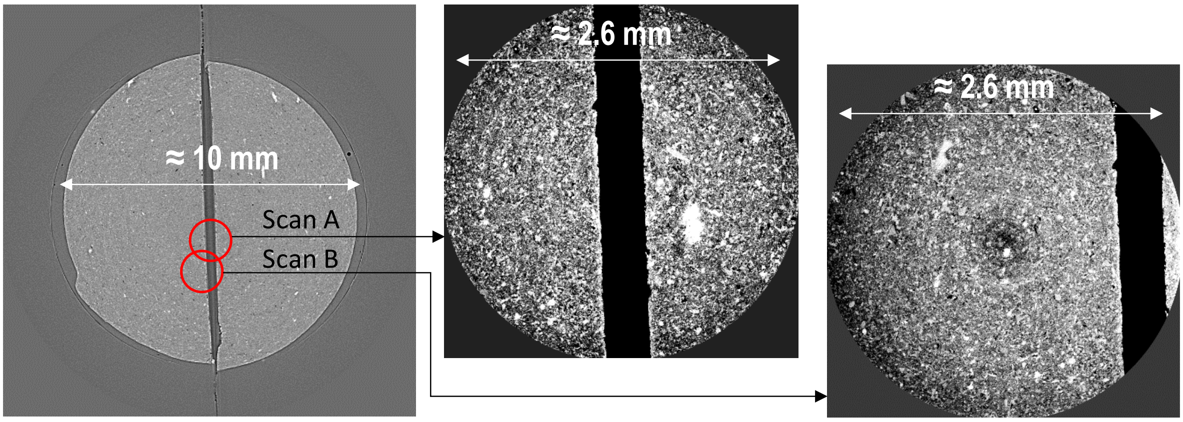

**Figure 18. set of X-ray tomographies obtained at the ESRF; (left) scan on the whole sample (voxel size 6 µm), (middle) high-resolution local scan (voxel size 0.7 µm) centred on the crack, (right) the same slightly off-centred from the crack.**

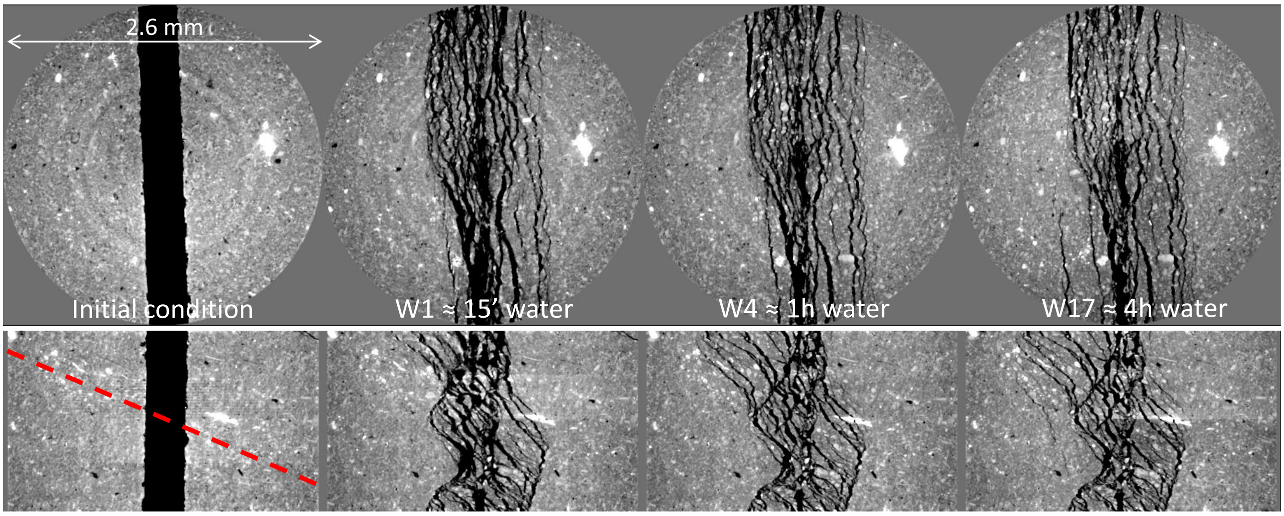

**Figure 19. X-ray images at different steps during test H2122 (U.A.), local tomography with voxel size 0.7 µm. Initial gap is 300 µm. The red dotted line in the bottom-left intact vertical cut shows the orientation of the natural bedding.**

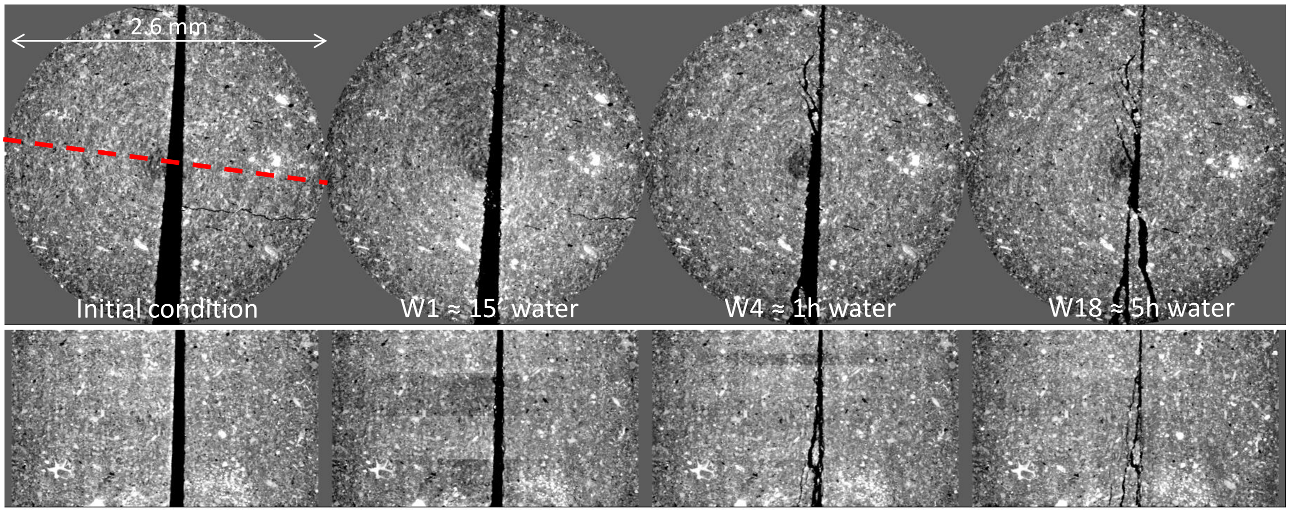

**Figure 20. X-ray images at different steps during test V3132 (U.A.), voxel size 0.7 µm. The red dotted line in the top-left intact horizontal cut shows the orientation of the natural bedding.**

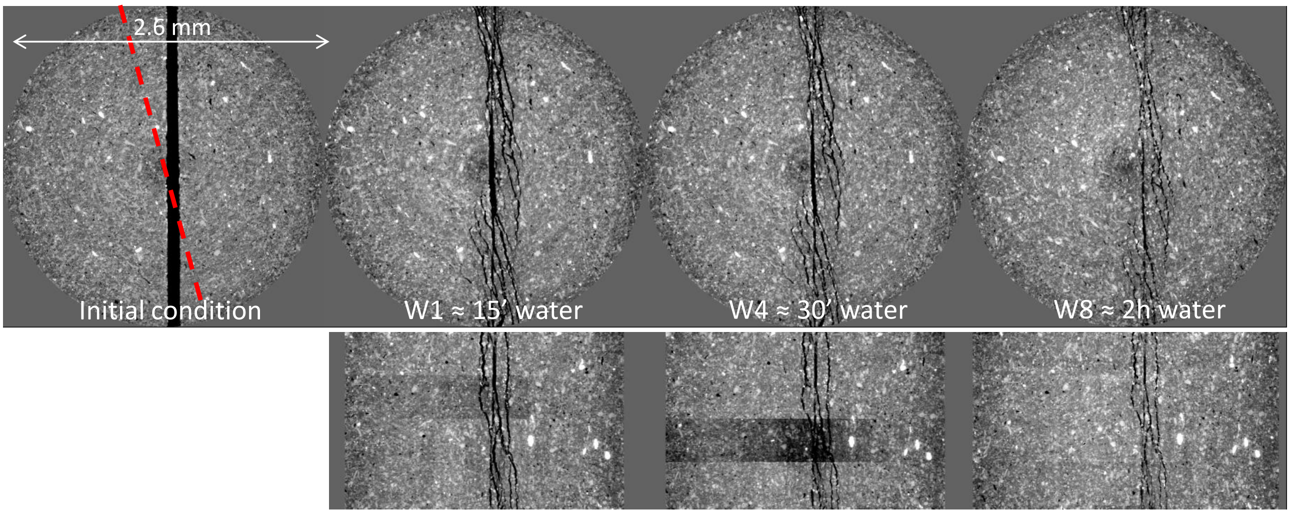

**Figure 21. X-ray images at different steps during test V4142 (U.A.), voxel size 0.7 µm. Initial mean gap is 75 µm. The red dotted line in the top-left intact horizontal cut shows the orientation of the natural bedding.**

At this scale and spatial resolution, the network of induced micro fractures is clearly visible. This highlights the micro mechanisms occurring behind the macro swelling behaviour detected at the larger (sample) scale. The macro swelling could appear to be the result of peeling (Figure 13), as theoretically discussed in the introduction (Figure 1), which is clearly visible here for the three tests, where the closure mechanism is dominated by the appearance of micro-cracks around the initial crack. For samples H2122 and V4142, the peeling of the material is strongly conditioned by the orientation of the bedding plane and mostly parallel to it. It appears essentially as a dense network of parallel micro-cracks, the opening of these cracks contributing to the reclosing of the initial crack. For sample H2122, if the bedding had been perpendicular to the crack, as expected during the preparation of the sample, the closure mode would probably have been quite different, as the peeling parallel to the bedding would not have been able to contribute to filling the main crack. This can be observed in sample V3132, the bedding being quite perpendicular to the crack. It appears that the network of cracks is much less dense than in the other two cases, with a lower reclosing efficiency. The orientation of these cracks corresponds to an intermediate orientation between the crack plane and the bedding plane.

The threshold technique was applied again with the purpose to understand if the sum of the sizes of the micro fractures at the end of the process was equivalent to the initial size of the discontinuity. Figure 22b shows the grey level profile along the sample diameter in the rectangular selection presented in Figure 22a at the beginning of the experiment and after 15 minutes, 1 and 4 hours. Based on this, the threshold was in this case chosen as 25000, with the purpose to include all the visible micro fissures. Thresholding was applied in the rectangular selection area represented in Figure 22c, and the result in terms of equivalent aperture is presented in Figure 22d. The equivalent total aperture remains roughly constant during the process, leading to the conclusion that the total void space available in the sample does not change significantly.

In accordance with permeability measurements realised during self-sealing tests and available in the literature, in such conditions, the hydraulic permeability is expected to reduce significantly with respect to the open fracture configuration. According to the cubic law for fracture permeability, the final hydraulic permeability of a net of N fractures having size $\delta/N$, $\delta$ being the size of the initial discontinuity, can be estimated as proportional to $1/N^2$. For instance, (Davy et al. 2007) concluded that water permeability increases of one or two orders of magnitude due to fractures, but than it goes back to the initial values of $10^{-21}$ m$^2$ after a few hours on injection. Similarly, Giot et al. 2018b showed a reduction in permeability of one order of magnitude, from $10^{-17}$ to $10^{-18}$ m$^2$.

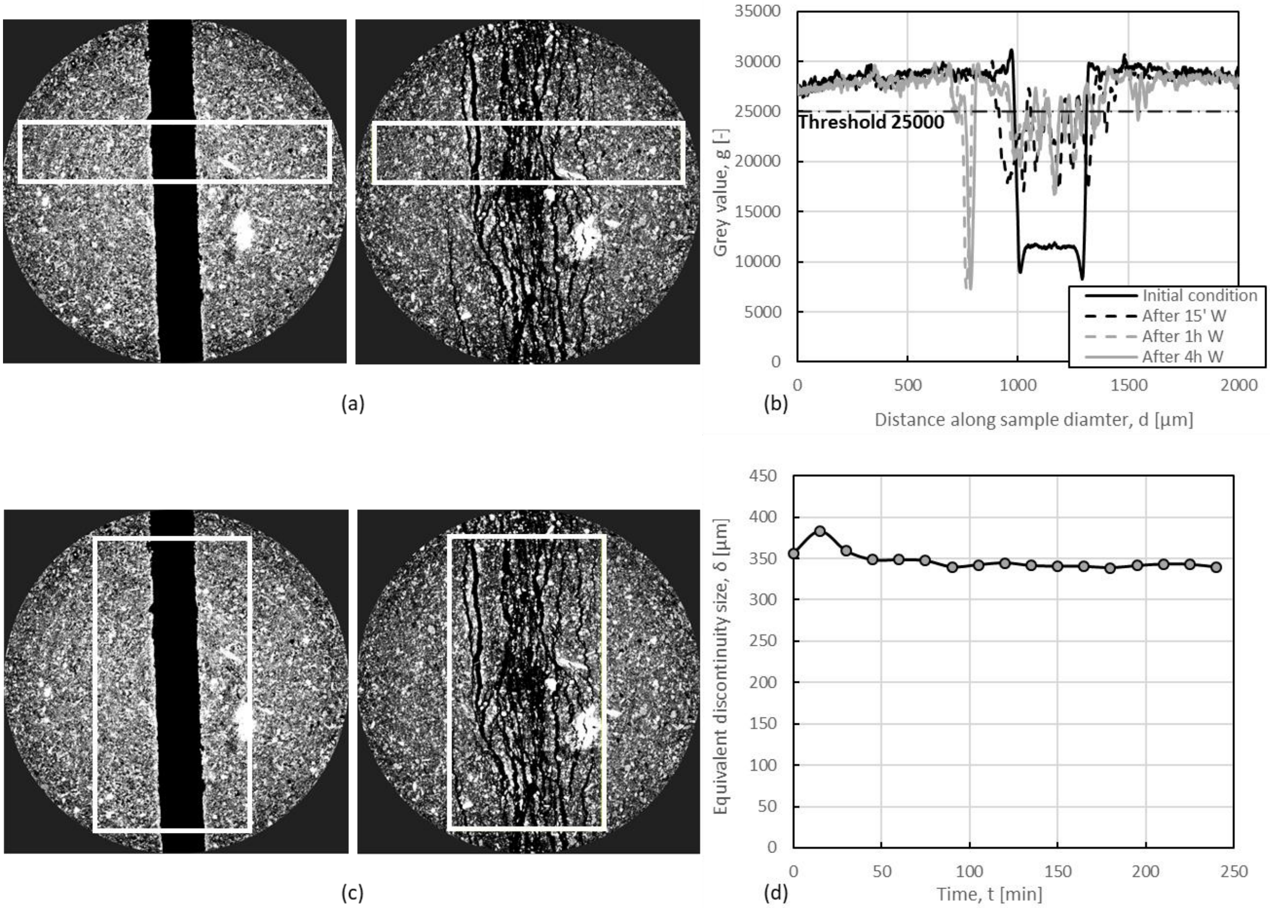

**Figure 22. Analysis of the open fracture size during the process: (a) selected area for the threshold choice, (b) greyscale profiles in the selected area, (c) thresholded area and (d) evolution of void space with time.**

In addition to the peeling mode occurring around the initial crack, there is also a diffuse deformation mechanism throughout the sample, which given the boundary conditions imposed on it (no or small displacements on the circumference), also contributes to the sealing process. This was also argued by Giot et al. 2018b, who observed a first quick swelling of the smectite clay minerals close to the crack, followed by swelling of the smectite clay minerals in the whole sample. Here, this was measured by digital volume correlation on the global scans of sample H2122. A progressive swelling propagates through the whole sample from the initial central crack (Figure 23). The deformation component shows a significantly larger deformation in the axial direction (z) of the sample than in the direction perpendicular to the crack (x), while the direction parallel to the crack (y) shows almost no deformation (Figure 24). This shows that the swelling is clearly anisotropic, dominated by the natural orientation of the bedding, and by the boundary conditions imposed on the sample. The swelling is highest in the direction perpendicular to the bedding. It is also significant in the direction perpendicular to the crack and contributes to the crack sealing process. The same observation can be done from sample V4142, with a progressive swelling through the sample (Figure 25). Swelling is significant in the direction perpendicular to both the initial crack and bedding (x), while it is vanishing in other directions (Figure 26).

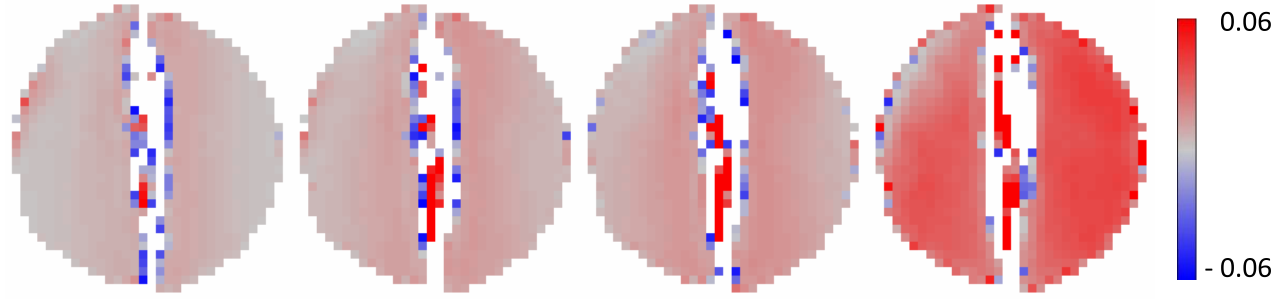

**Figure 23. Field of volume strain measured at different steps of the test H2122, from the low resolution (6um) global scans (positive sign means expansion).**

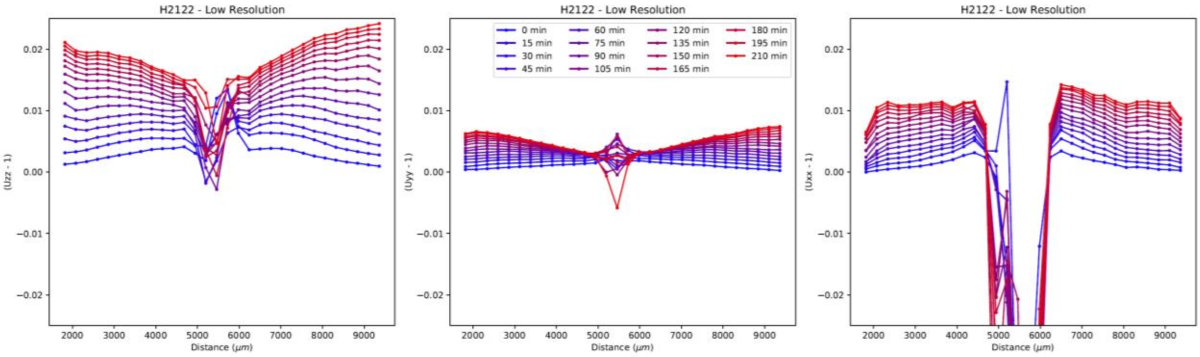

**Figure 24. Profiles of deformation of the test H2122 in the z, y and x direction corresponding to a profile perpendicular to the crack. The noisy data in the central zone (peeling area) are not significant.**

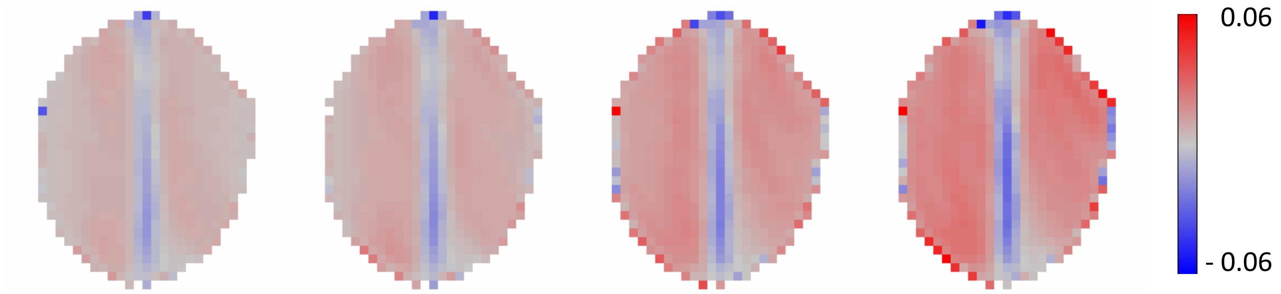

**Figure 25. Field of volume strain measured at different steps of the test V4142, from the low resolution (6um) global scans**

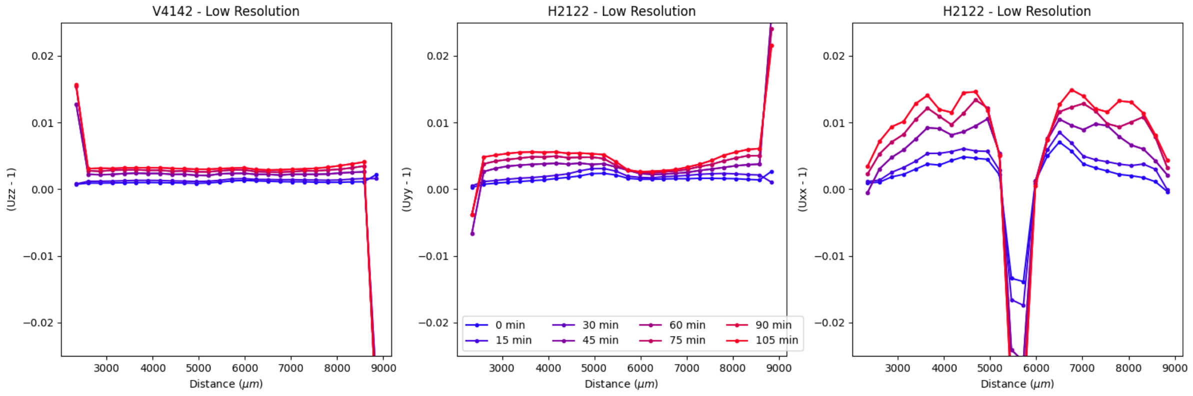

**Figure 26. Profiles of deformation of the test 4142 in the z, y and x direction corresponding to a profile perpendicular to the crack. The noisy data in the central zone (peeling area) are not significant.**

# 8 Conclusions

The self-sealing response of COx claystone was experimentally investigated through x-ray tomography. The experimental campaign performed was designed to study the influence of a number of parameters on the self-sealing behaviour of the COx claystone, such as different geological units, size of the discontinuity, different hydraulic paths, mutual orientation of the bedding plane and fractures. As highlighted by Giot et al. (2018a), two phases are usually observed in self-sealing, i.e. a fast closure of the fracture corresponding to a rapid decrease of water permeability and a slow process that leads to a further slow decrease of water permeability. The observations made in this study are representative of short-term evolution of the material. Comparing the results obtained, the following conclusions can be drawn.

Concerning the geological units, the results were strongly dependent on the geological unit from which the samples came from. Samples coming from the clay unit (U.A.) were definitely more reactive than those of the transition unit (U.T.). This was linked to the substantially different mineralogy: U.A. samples were richer in active (smectite) clay, while U.T. samples were richer in carbonates (Table 1). High carbonates content were also associated to very low porosity of these samples, responsible of limiting the access of water to the possibly existing swelling clays.
The sealing process can be broken down into two phenomena. In the area adjacent to the crack, a peeling phenomenon opens up micro-cracks that preferentially run parallel to the material bedding. These cracks contribute to the filling of the main crack. In addition, around the peeling zone, the material shows a diffuse swelling. In the case of oedometer conditions (radial displacement prevented on the circumferential edge of the sample), this swelling contributes to the sealing of the main crack.

Concerning the size of the discontinuity, in small fractures (75 to 150 μm) the self-sealing phenomenon stabilised rapidly, showing an almost complete closure, with no visible peeling effect at the resolution of the images realised in this study (voxel size 15 μm). This is likely to be related to smaller space for deformation available as well as to the related quantity of water provided during saturation. Note however that a test with an initial small fracture performed with high-resolution tomography (voxel size 0.7 μm) show a peeling effect with very thin fractures. In samples with larger initial discontinuities, the peeling effect was much more evident, even at the same resolution. Higher resolution images (voxel size 0.7 μm) highlighted this effect at the discontinuity lips, showing that the closure of the main fracture is actually associated with the de-structuration of the material and the consequent creation of a network of smaller cracks. However, in such conditions the hydraulic permeability is still expected to be significantly reduced with respect to the open fracture configuration (Davy et al. 2007, Giot et al. 2018b). This was confirmed by the analysis of the evolution of the bulk density around the discontinuity (peeling area) during saturation: it evolved towards the one of the intact material, without completely reaching it. It was found that, at a given specimen size, the bigger the initial discontinuity, the lower the percentage of recovery in density, which was however always over 88% (Figure 17).

The hydraulic path itself has an impact. The reaction of all samples during the phases of saturation by water vapour was very limited, at least for the duration of these experiments. The response of reactive samples to liquid water was on the contrary very fast, independently on the fact that it was preceded by a vapour or drying phase. However, samples subjected to drying first showed possibly a more evident peeling effect. During drying phases, all samples showed an opening of the fractures, which was most important in samples that were previously subjected to saturation by liquid water (Figure 15).

Concerning the orientation of the bedding plane, the specimens cut with the fracture parallel to the bedding plane showed a more significant reaction with respect to the one cut with the facture perpendicular to the bedding plane. In particular, the peeling cracks appear roughly parallel to the bedding plane, as expected. In addition, the swelling of the material in the area outside the peeling zone shows an anisotropic swelling, which is significantly greater in the direction orthogonal to the bedding. If the bedding is parallel to the fracture, this swelling clearly contributes with more efficiently to the sealing. For a fracture perpendicular to the bedding, there can be a peeling phenomenon, but less strong than in the parallel case, with an intermediate orientation between the fracture and the bedding.

The obtained results are perfectly in accordance with the conclusion provided by Menaceur et al. (2016) on the evolution of COx microstructure during hydration. They found that, the reduction of suction to zero (as in the W-phases of this study), allows to place a third and even a fourth layer of water molecules between the smectite layers. According to these authors, this induces a significant change in the porosity of the material, with a simultaneous creation of a network of saturated cracks. The global swelling observed at the macro scale results from the combination of these two phenomena. It is concluded that the physico-chemical interactions are of primary importance in governing the micro structural behaviour of the claystone, being able to mobilise an energy strong enough to break the inter-particle bonding present in the initial state. In this sense, these physico-chemical phenomena provide a strong contribution to the self-sealing.

## 9 Acknowledgements

The authors would like to thank Andra for the financial support and in particular Nathalie Conil and Jean Talandier for the useful discussions. The collaboration with the colleagues of the Isterre laboratory, Nathaniel Findling and Bruno Lanson, for the mineralogical analyses was also much appreciated. The authors would also like to thank Elodie Boller (ESRF) for her assistance at the ESRF. Laboratoire 3SR is part of the LabEx Tec 21 (Investissement d'avenir — grant agreement n. ANR-11-LABX-0030).

## 10 References

Alheid, H.J., Kontar, K., and Trick, T. 2004. Engineered barrier emplacement (EB), experiment in opalinus clay: hydrogeological characterisation of the EDZ. Mont Terry Project Technical Note. Switzerland.

Bernier, F., Li., X., Bastiaens, W., Ortiz, L., van Geet, M., Wouters, L., Frieg, B., Blumling, P., Desrues, J., Viggiani, G., Coll, C., Chanchole, S., De Greef, V., Hamza, R., Malinsky, L., Vervoort, A., Vanbrabant, Y., Debecker, B., Verstraelen, J., Govaerts, A., Wevers, M., Labiouse, V., Escoffier, S., Mathier, J.F., Gastaldo, L., and Buhler, C. 2004. SELFRAC - Fractures and self-healing within the excavation disturbed zone in clays. Final report. Brussel.

Bock, H., Dehandschutter, B., Derek Martin, C., Mazurek, M., de Haller, A., Skoczylas, F., and Davy, C. 2010. Self-sealing of fractures in argillaceous formations in the contaxt of geological disposal of radioactive waste. OECD.

Bossart, P., Meier, P.M., Moeri, A., Trick, T., and Mayor, J.C. 2002. Geological and hydraulic characterisation of the excavation disturbed zone in the Opalinus Clay of the Mont Terri Rock Laboratory. Engineering Geology, **66**(1–2): 19–38. doi:10.1016/S0013-7952(01)00140-5.

Conil, N., Talandier, J., Djizanne, H., de La Vaissière, R., Righini-Waz, C., Auvray, C., Morlot, C., and Armand, G. 2018. How rock samples can be representative of in situ condition: A case study of Callovo-Oxfordian claystones. Journal of Rock Mechanics and Geotechnical Engineering,. Elsevier Ltd. doi:10.1016/j.jrmge.2018.02.004.

Davy, C.A., Skoczylas, F., Barnichon, J.D., and Lebon, P. 2007. Permeability of macro-cracked argillite under confinement: Gas and water testing. Physics and Chemistry of the Earth, **32**(8–14): 667–680. doi:10.1016/j.pce.2006.02.055.

Delay, J., Vinsot, A., Krieguer, J.M., Rebours, H., and Armand, G. 2007. Making of the underground scientific experimental programme at the Meuse/Haute-Marne underground research laboratory, North Eastern France. Physics and Chemistry of the Earth, **32**(1–7): 2–18. doi:10.1016/j.pce.2006.04.033.

Distinguin, M., and Lavanchy, J.M. 2007. Determination of hydraulic properties of the Callovo-Oxfordian argillite at the Bure site: Synthesis of the results obtained in deep boreholes using several in situ investigation techniques. Physics and Chemistry of the Earth, **32**(1–7): 379–392. doi:10.1016/j.pce.2006.02.056.

Giot, R., Auvray, C., Conil, N., and de La Vaissière, R. 2018a. Multi-stage water permeability measurements on claystone by steady and transient flow methods. Engineering Geology, **247**(October):27–37, doi:10.1016/j.enggeo.2018.10.019.

Giot, R., Auvray, C., Talandier, J., Self-sealing of claystone under X-ray nanotomography. Geological Society of London, 2018, SP482.4. doi:10.1144/SP482.4.

Kim, H., Prezzi, M., and Salgado, R. 2016. Calibration of Whatman Grade 42 Filter Paper for Soil Suction Measurement. Canadian Journal of Soil Science, (November). doi:10.1139/cjss-2016-0064.

Leroy, P., Revil, A., Altmann, S., and Tournassat, C. 2007. Modeling the composition of the pore water in a clay-rock geological formation (Callovo-Oxfordian, France). Geochimica et Cosmochimica Acta, **71**(5): 1087–1097. doi:10.1016/j.gca.2006.11.009.

Menaceur, H., Delage, P., Minh, A., and Jean, T. 2016. The Status of Water in Swelling Shales : An Insight from the Water Retention Properties of the Callovo-Oxfordian Claystone. Rock Mechanics and Rock Engineering, doi:10.1007/s00603-016-1065-2.

Mitchell, J.K., and Soga, K. 2005. Fundamentals of soil behavior. John Wiley.

Mohajerani, M., Delage, P., Monfared, M., Tang, A.M., Sulem, J., and Gatmiri, B. 2011. Oedometric compression and swelling behaviour of the Callovo-Oxfordian argillite. International Journal of Rock Mechanics and Mining Sciences, **48**(4): 606–615, doi:10.1016/j.ijrmms.2011.02.016.

Pham, Q.T., Vales, F., Malinsky, L., Nguyen Minh, D., and Gharbi, H. 2007. Effects of desaturation-resaturation on mudstone. Physics and Chemistry of the Earth, **32**(8–14): 646–655. doi:10.1016/j.pce.2006.03.012.

Saiyouri, N., Hicher, P.Y., and Tessier, D. 1998. Microstructural analysis of highly compacted clay swelling. 2nd Int. Conf. on Unsaturated Soils, **1**(January 1998): 119–124.

Stavropoulou, E., Andò, E., Roubin, E., Lenoir, N., Tengattini, A., Briffaut, M., and Bésuelle, P. 2020. Dynamics of Water Absorption in Callovo-Oxfordian Claystone Revealed With Multimodal X-Ray and Neutron Tomography.

Frontiers in Earth Science, **8**(March). doi:10.3389/feart.2020.00006.

Stavropoulou, E., Andò, E., Tengattini, A., Briffaut, M., Dufour, F., Atkins, D., and Armand, G. 2018. Liquid water uptake in unconfined Callovo Oxfordian clay-rock studied with neutron and X-ray imaging. Acta Geotechnica, **4**: 1–15. doi:10.1007/s11440-018-0639-4.

Viggiani, G., Andò, E., Takano, D., and Santamarina, J.C. 2015. Laboratory X-ray tomography: A valuable experimental tool for revealing processes in soils. Geotechnical Testing Journal, **38**(1): 61–71. doi:10.1520/GTJ20140060.

Wan, M., Delage, P., Tang, A.M., and Talandier, J. 2013. Water retention properties of the Callovo-Oxfordian claystone. International Journal of Rock Mechanics and Mining Sciences, **64**: 96–104., doi:10.1016/j.ijrmms.2013.08.020.

Zhang, C., and Rothfuchs, T. 2008. Damage and sealing of clay rocks detected by measurements of gas permeability. **33**: 363–373. doi:10.1016/j.pce.2008.10.013.

Zhang, C.L., Rothfuchs, T., Su, K., and Hoteit, N. 2007. Experimental study of the thermo-hydro-mechanical behaviour of indurated clays. Physics and Chemistry of the Earth, **32**(8–14): 957–965. doi:10.1016/j.pce.2006.04.038.